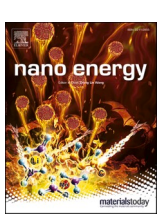
ELSEVIER

Contents lists available at ScienceDirect

Nano Energy

journal homepage: www.elsevier.com/locate/nanoen





Tuning core-shell structural architecture for high-performance Li-Mn-O layered oxides

Weiyuan Huang a,1 , Xiaoyuan Li a,1 , Wenguang Zhao a , Chen Zhu a , Hengyu Ren a , Haibiao Chen b , Feng Pan a,* , Mingjian Zhang a,*

- ^a School of Advanced Materials, Peking University, Shenzhen Graduate School, Shenzhen 518055, China
- ^b Institute of Marine Biomedicine, Shenzhen Polytechnic, Shenzhen 518055, China

ARTICLE INFO

Keywords: Lithium-ion batteries Li-Mn-O layered oxides Post-annealing Core-shell structural architecture Structure stability

ABSTRACT

Being free of cobalt and nickel, Li-Mn-O layered oxides are considered as one of the most promising candidate cathodes due to the low cost and high specific capacity. The relatively poor thermal stability of Li-Mn-O layered oxides can lead to battery safety issues, and thus needs to be improved for practical applications. Herein, we systemically investigated the heat-induced structural/chemical evolution of a Li-Mn-O material, revealing a two-step phase transition process through concurrent Li and O loss, heterogeneously occurring in the bulk and at the surface of the primary particles. Based on the understanding of structural change, two new Li-Mn-O materials with different core-shell microstructures, one with a spinel shell and another with an orthorhombic shell, were synthesized. Experimentally, the one with the spinel shell achieved an ultrahigh decomposition temperature of ~300 °C, which is vital for battery safety. This material also exhibited greatly enhanced cycling stability and rate capability due to the protection role of the spinel shell. This work paves new routes to produce high-performance cathode materials with various heterostructure architectures through the tunning temperature-sensitive structure evolution process.

1. Introduction

Due to the limited resources of cobalt and nickel, the Li-Mn-O system without any cobalt or nickel is greatly attractive in terms of materials cost compared to Co-based and Ni-rich layered cathodes for Li-ion batteries. [1-6] The Li-Mn-O system includes two stoichiometric types, Li₂MnO₃ and LiMnO₂. Li₂MnO₃ is electrochemically unstable and suffers serious structure degradation due to irreversible O redox. [7-10] LiMnO₂ is a thermodynamic metastable phase and thus is difficult to be produced by the traditional sintering method. [11,12] In 1996, Armstrong and Bruce successfully prepared stoichiometric LiMnO2 from \mbox{NaMnO}_2 by a unique ion exchange method, and the material exhibited a high capacity of 270 mA h g⁻¹ and good cycling stability. [13] In 2020, Xia's group developed another electrochemical ion exchange method to obtain stoichiometric LiMnO2 with a layered/spinel intergrown heterostructure, which showed a high specific capacity of 254 mA h g⁻¹ as well as excellent rate and cycling performance. [14] Ion exchange methods are also applied to prepare a series of non-stoichiometric

Li-Mn-O layered oxides. In 2020, Xia's group synthesized O2-type layered Li $_{0.78}$ [Li $_{0.24}$ Mn $_{0.76}$]O $_2$ nanowires and they achieved a high capacity of 275 mA h g $^{-1}$ at 0.1 C and good rate capability (200 mA h g $^{-1}$ at 15 C). [15] Zhou's group also reported an O3-type Li $_{0.6}$ [Li $_{0.2}$ Mn $_{0.8}$]O $_2$ by the ion exchange method, and the material achieved a high capacity of 329 mA h g $^{-1}$ at 10 mA g $^{-1}$ and good cycling performance at a higher current density of 300 mA g $^{-1}$. [16] These reports indicate that Li-Mn-O layered oxides have become one of the interests of the research on cathode materials with high energy density and low cost.

Although layered Li-Mn-O materials have shown excellent electrochemical performance, studies on the basic physical/chemical properties of these materials are still insufficient. [17–20] Especially, thermal stability, which is a key factor to affect battery safety, is not well understood. [21–25] Typically these materials are produced using ion exchange at a relatively low temperature (280 °C), they might not be thermally stable at a higher temperature during use and are not validated before use. [26] Therefore, validating the thermal property of Li-Mn-O oxides prepared by an ion exchange method is necessary for the

E-mail addresses: panfeng@pkusz.edu.cn (F. Pan), zhangmj@pkusz.edu.cn (M. Zhang).

^{*} Corresponding authors.

¹ These authors contributed equally to this work.

safe operation of batteries.

In this work, we prepared a new Li-rich layered oxide $\rm Li_{1.11}Mn_{0.76}O_2$ by the ion exchange method and used it as a model material to systemically investigate the thermal property. Especially, the whole process of heat-induced microscopic/local structure evolution was thoroughly investigated by combining multiple macroscopic/microscopic characterization techniques. Based on the new understanding of the process, two core-shell structured Li-Mn-O layered oxides, one with a spinel shell and the other with an orthorhombic shell, were synthesized. The Li-Mn-O oxide with a spinel shell exhibited enhanced thermal stability, cycling stability, and rate capability, benefitting from the unique core-shell structure. This work provides a new opportunity in the controllable synthesis of high-performance lithium-ion battery cathode materials with composite phase microstructures.

2. Results and discussion

2.1. Bulk phase transition upon annealing

The Li_{1.11}Mn_{0.76}O₂ sample synthesized by the ion exchange method is labeled as LMO. Fig. 1a shows the schematic illustration of the production of a core-shell structural architecture through annealing. *Ex situ* XRD was used to track the bulk phase transition when LMO was annealed from room temperature to 850 °C. As shown in Fig. S1, there is no change in the XRD patterns below 250 °C, indicating no obvious phase transition. When the temperature rose to 350 °C, three weak peaks in the range of 45–65° (marked by the stars) emerged, which are indexed to a typical LiMn₂O₄-like spinel phase with a space group *Fd-3m*. Besides, the superlattice peak at 21° gradually intensified to some extent as the temperature increased. With the temperature further increasing to 650 °C, the (003)_L peak splits into two peaks, of which the new one at a lower angle is attributed to the spinel phase. In the meanwhile, other peaks of the spinel phase become obvious. At 750 and 850 °C, two new

phases LiMnO₂-like monoclinic (space group C2/m) and LiMnO₂-like orthorhombic (space group Pmnm) were confirmed by further analysis. In one word, a very complicated phase transition process, from the initial monoclinic layered phase (Li₂MnO₃-like) to the spinel phase (LiMn₂O₄-like), and finally to new monoclinic and orthorhombic phases (LiMnO₂-like), occurred upon annealing.

To accurately determine the phase compositions, Rietveld refinements were performed on the above individual XRD patterns (Fig. S2, Table S2, S3). Detailed phase composition data are summarized in Fig. 1b. The entire phase transition process consists of three stages divided by two transitions, at 300 and 700 $^{\circ}$ C, respectively. From room temperature to 250 °C, the sample preserves the pure monoclinic phase without any changes. Above 250 °C, a spinel phase appears, and its content increases from 16.61 wt % to 29.95 wt % with the temperature increasing from 350 °C to 450 °C, accompanied by the decrease in the content of the monoclinic phase. From 450-650 °C, the phase composition changes little, and this is a rather wide temperature window for the two-phase composite to be stable. Above 650 °C, another phase transition process takes place, in which the spinel phase disappears and the monoclinic content decreased sharply, followed by the occurrence of both LiMnO₂-like monoclinic phase and orthorhombic phase. From 750° to 850°C, the content of LiMnO₂-like monoclinic phase continues to decrease while the content of LiMnO2-like orthorhombic phase increases, indicating a phase transition from the monoclinic phase to the orthorhombic phase. These results are consistent with the previous report, which claimed that monoclinic LiMnO2 is a metastable phase, and orthorhombic LiMnO₂ is the thermodynamically stable phase. [27] Thermogravimetric analysis (TGA) was further conducted to complement the phase transition study. Matching the phase evolution revealed by XRD, the weight curve can also be divided into three plateaus by two major weight loss steps. As shown in Fig. 1c and Table S4, the 1st weight loss of 3.4% occurred from 200 °C to 300 °C, corresponding to the 1st phase transition from the initial monoclinic layered phase to the spinel

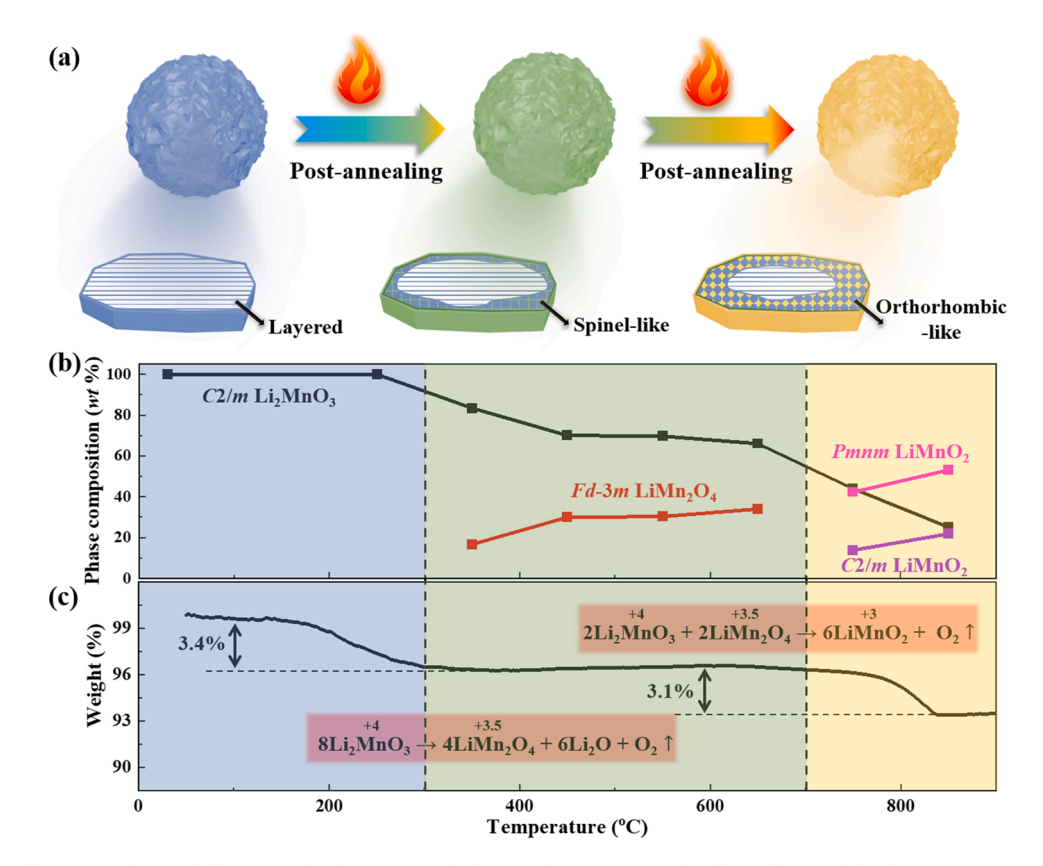


Fig. 1. (a) Schematic illustration of core-shell structural architecture with the annealing treatment. (b) The evolution of the phase composition with the temperature based on Rietveld refinements of the corresponding XRD patterns. (c) TGA analysis of pristine LMO.

phase. The sample weight remained almost constant from 300 $^{\circ}$ C to 700 $^{\circ}$ C, which corresponds to the co-existence of both phases. The 2nd weight loss of 3.1% started from 700 $^{\circ}$ C, roughly matching the 2nd phase transition to LiMnO₂-like monoclinic phase and orthorhombic phase. Since the XRD was conductive *ex situ*, the observed transformation temperatures were not strictly aligned with the TGA curve.

The two phases transitions can be described using the reaction formulas in Fig. 1c. The 1st one is the decomposition of Li₂MnO₃ into the spinel LiMn₂O₄, accompanied by Li and O loss in the forms of Li₂O and O₂. The 2nd one is the complex decomposition reaction between Li₂MnO₃ and LiMn₂O₄ to produce LiMnO₂ and O₂. Both reactions induced the continuous reduction of Mn from $+4\ to+3$.

In Fig. 2a, TGA-MS was used to trace the gas evolution from 50 °C to 500 °C. Both O₂ and CO₂ were detected in the weight loss range, which could be related to the loss of lattice oxygen from the bulk and the decomposition of trace residual carbonate or hydrocarbonate on the particle surface. To detect the valence change of Mn, XPS analyses were performed on the corresponding samples. As shown in Fig. 2b, two distinct peaks at about 641.6 eV and 642.6 eV were observed in the pristine sample, and they can be assigned to Mn³⁺ and Mn⁴⁺, respectively. With the temperature increasing, another peak at 640.5 eV gradually appeared. This peak is associated with Mn²⁺, indicating the continued reduction of Mn. Quantitative analysis was carried out by the peak fitting as shown in Fig. 2b. The initial ratio between the peak areas of Mn³⁺ and Mn⁴⁺ was nearly 1: 2, which is well consistent with the average valence + 3.72. As the temperature increased to 450 $^{\circ}$ C, the molar ratio of Mn³⁺/Mn⁴⁺ slowly increased, which corresponds to the Mn reduction as the initial monoclinic phase transformed to the spinel phase. Above 550 °C, Mn²⁺ started to appear and its content gradually grew with the temperature. Mn²⁺ could be from MnO formed on the particle surface, in consideration of the surface-sensitivity of XPS. The Mn X-ray absorption near edge spectra (XANES) were collected for the pristine, 450 °C and 750 °C samples. As shown in Fig. S3, the linear

fitting of Mn XANES spectra deduces the average valences of Mn as + 3.81, + 3.66, and + 3.54, respectively, which are consistent with the trend from XPS results. O 1 s spectra are illustrated in Fig. 2c. Besides the main peak of oxide at around 529.3 eV, a weak and broad peak at around 531.2 eV should come from the surface Li₂CO₃ or LiHCO₃. To explore when the surficial Li₂CO₃ or LiHCO₃ formed during the synthesis of LMO, we collected the O 1 s XPS spectrum of Na precursor and molten salt after ion-exchange (Fig. S4). It is clear, there is a broad peak at around 531 eV for both samples, assigned to the formation of surficial carbonate species during the high-temperature calcination. These carbonate species cannot be fully removed after water washing, [28-30] and would be reformed by the reaction between the Li⁺ ions-containing species in the residual water and CO₂/H₂O during the drying process. [31,32] These carbonate species could not be removed during the ion exchange and would release CO₂ during the subsequent heating process. The intensity of carbonate/hydrocarbonate peak decreases with the temperature increasing from 250 °C to 650 °C, which is consistent with the TGA-MS results. As the temperature further increased to above 750 °C, the peak of carbonate/hydrocarbonate intensified again. They come from the reaction between Li₂O (generated at the particle surface upon heat-induced structure evolution process in Table S4) and CO₂/H₂O in the air during the sample storage and transfer.

2.2. Local structural transition upon annealing

As a complement to the bulk phase transition revealed by XRD, temperature-resolved TEM was adopted to track the local structure change upon the annealing process. Fig. S5 shows the TEM images of the secondary particles when heating at elevated temperatures. The selected secondary particle shrank upon 550 $^{\circ}$ C and underwent a significant morphology change upon 700 $^{\circ}$ C. Fig. S6 exhibits the HRTEM images of a selected region at the surface of a primary particle. Obviously, this selected region also experienced significant morphology changes upon

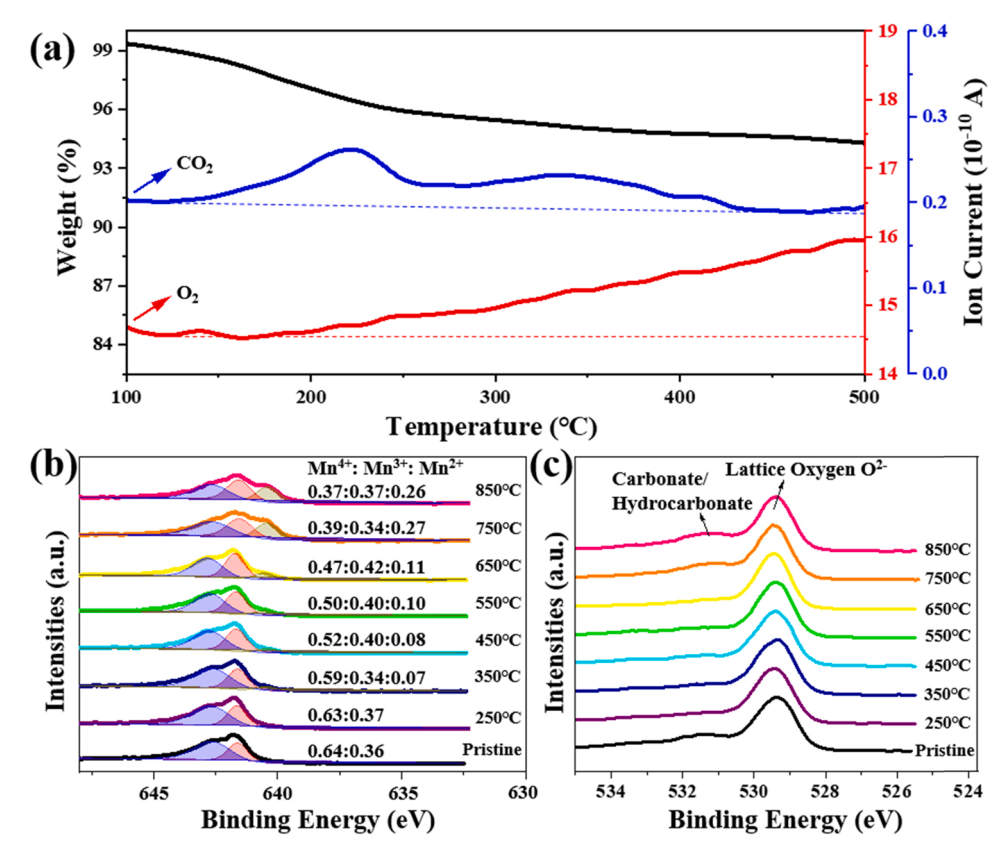


Fig. 2. (a) TGA-MS analysis during the annealing process of LMO. (b), (c) Mn 2p and O 1 s XPS for the samples after annealing at different temperatures.

heating. To better illustrate the local structure change, fast Fourier transformation (FFT) maps were generated to identify the different phases as shown in Fig. 3a-f. As shown in Fig. 3a, the chosen area is assigned to the LiMn₂O₄-like spinel phase, and three diffraction spots are indexed to the $(-220)_S$, $(-131)_S$, and $(111)_S$ planes based on the d spacings and the angles between them. When the temperature rose to 350 °C (Fig. 3b), another $(111)_S$ spot appeared on the same diffraction ring passing the previous $(111)_S$ spot, which hints that a new spinel domain formed in this selected region. When the temperature further increased to 450 °C (Fig. 3c), the spinel phase was preserved, but the diffraction spots, especially $(-131)_S$ spot split into multiple spots in comparison with that in Fig. 3a, indicating that the initial spinel domain was divided into more spinel domains. In addition to these diffraction spots, the diffraction rings marked by the green circles gradually became

clearer from 250 °C to 450 °C, indicating an amorphous intermediate phase was involved during the phase transition. When the temperature further reached 550 °C, the diffraction pattern in Fig. 3d changed and can be indexed to LiMnO₂-like monoclinic phase with three interesting diffraction spots indexed to the $(001)_{\rm M}$, $(1-10)_{\rm M}$, and $(1-11)_{\rm M}$ planes. This temperature for the phase transition is much lower than that observed by XRD (750 °C), which may be due to the high vacuum of the TEM. When the temperature was elevated to 650 °C and 700 °C, a new set of diffraction spots can be detected and they were assigned to the orthorhombic phase (Fig. 3e, f). Three representative diffraction spots were indexed to $(100)_{\rm O}$, $(120)_{\rm O}$, and $(320)_{\rm O}$ planes.

Overall, a phase transition process was observed locally at the surface of a single primary particle, with a trend similar to that revealed by the XRD results. What is different is that local area observation cannot

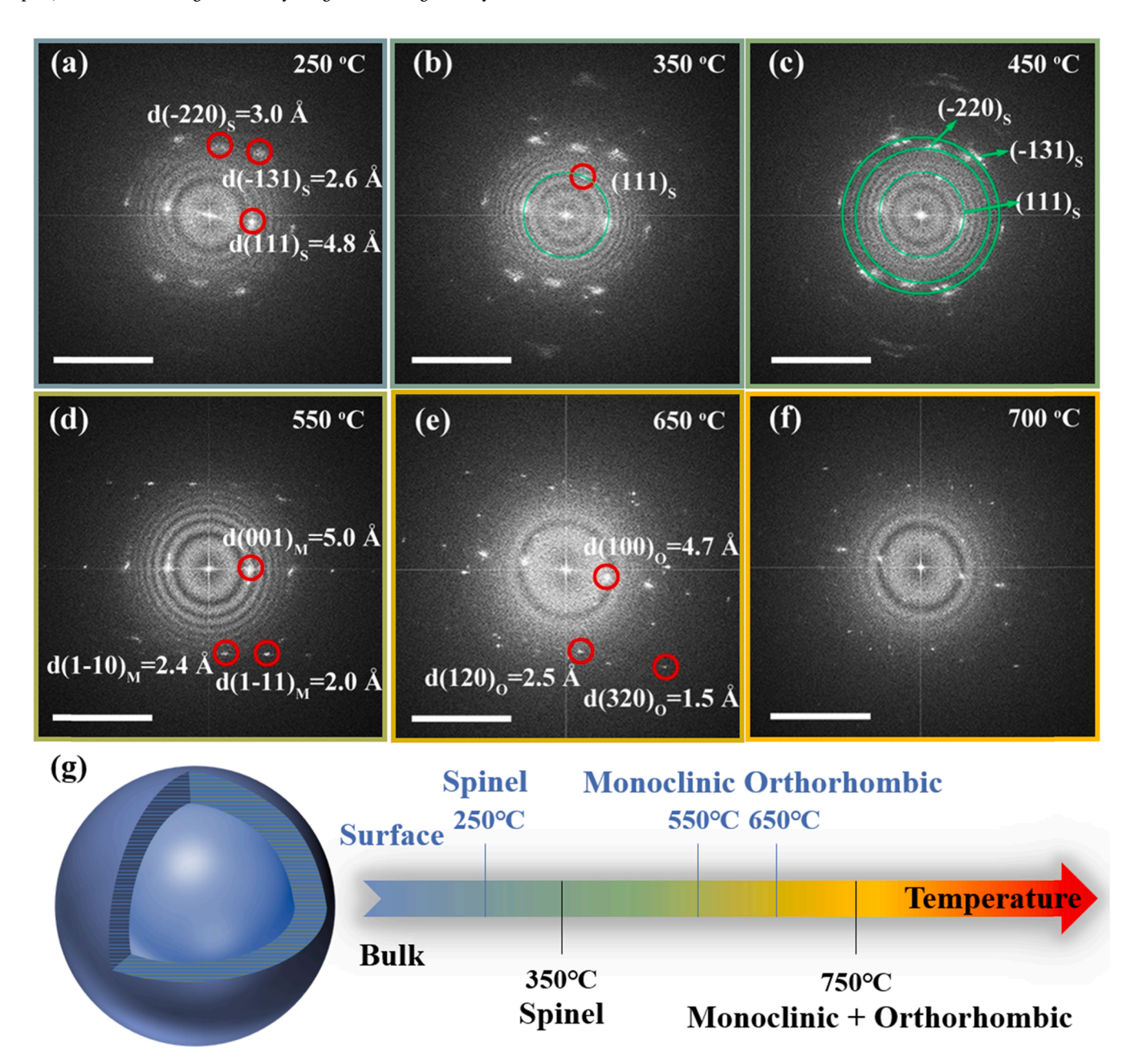


Fig. 3. FFT maps from TEM images recorded at 250 (a), 350 (b), 450 (c), 550 (d), 650 (e), and 700 °C (f). The corresponding TEM images are deposited in Fig. S5. The diffraction spots marked by red circles are indexed to the corresponding phases. The subscripts S, M, and O represent the spinel phase (*Fd-3m*), the monoclinic phase (*C2/m*), and the orthorhombic phase (*Pmnm*), respectively. The green circles are used to correlate multiple domains with the same spinel phase. All the scale bars are set 5 1/nm. (g) Schematic illustration to compare the phase transition processes in the bulk and at the surface, which come from the *ex situ* XRD results and *in situ* TEM results, respectively. (For interpretation of the references to colour in this figure legend, the reader is referred to the web version of this article.)

reflect the percentage of transformation. There appears to be a gradient of transition from the bulk to the surface of the particle. The scheme in Fig. 3 g summarizes the structural evolution processes that concurrently occurred in the bulk and at the surface of a single primary particle, as postulated from the ex situ XRD and in situ TEM, respectively. At the surface, the transition from the initial monoclinic phase to the spinel phase happens at 250 $^{\circ}$ C, or 100 $^{\circ}$ C lower than that in the bulk (350 $^{\circ}$ C). The transformation to LiMnO2-like monoclinic phase takes place at 550 °C, and the transformation to LiMnO2-like orthorhombic phase takes place at 650 °C, also 100 °C lower than that in the bulk (750 °C). The difference in the transition temperature can be explained by the different degrees of Li and O loss from the surface and the bulk. Initially, oxygen is lost from the particle surface, accompanied by lithium diffusing out to form amorphous Li₂O. Since the lithium is deficient at the particle surface, Mn ions replace Li⁺ ions in the tetrahedral sites to form a spinel phase, leading to a core-shell structure, with a core of layered oxide and a shell of spinel. At elevated temperatures, 650 °C and 750 °C, Li⁺ ions tend to diffuse from the layered core to the spinel shell to form the LiMnO₂-like monoclinic and orthorhombic phases. LiMnO₂like monoclinic phase is a thermodynamically unstable phase, and it would finally transform to the thermodynamically stable orthorhombic phase.

2.3. Constructing core-shell structure of as-prepared LMO

After recognizing the delayed transformation in the bulk phase, we intentionally constructed core-shell particles from LMO by simply annealing the material at different temperatures. Specifically, we selected two annealing temperatures, 450 °C and 750 °C, to produce two different core-shell materials for further investigation. Fig. 4a shows the XRD pattern and the corresponding Rietveld refinement of assynthesized LMO powder. All of the diffraction peaks can be well indexed and the superlattice peak at around 21° is considered as a typical character of Li-rich layered oxides. The morphology was observed by SEM (Fig. S7a). The secondary particles are spherical-like with an average diameter of about 1 μ m, composed of lots of primary particles with a size around 30–100 nm. The HRTEM image in Fig. 4d shows lattice fringe with a *d*-spacing of about 4.9 Å corresponding to the (001)_L plane of the layered phase, and the FFT map in the inset exhibits the typical diffraction pattern along with the c^* direction of the layered

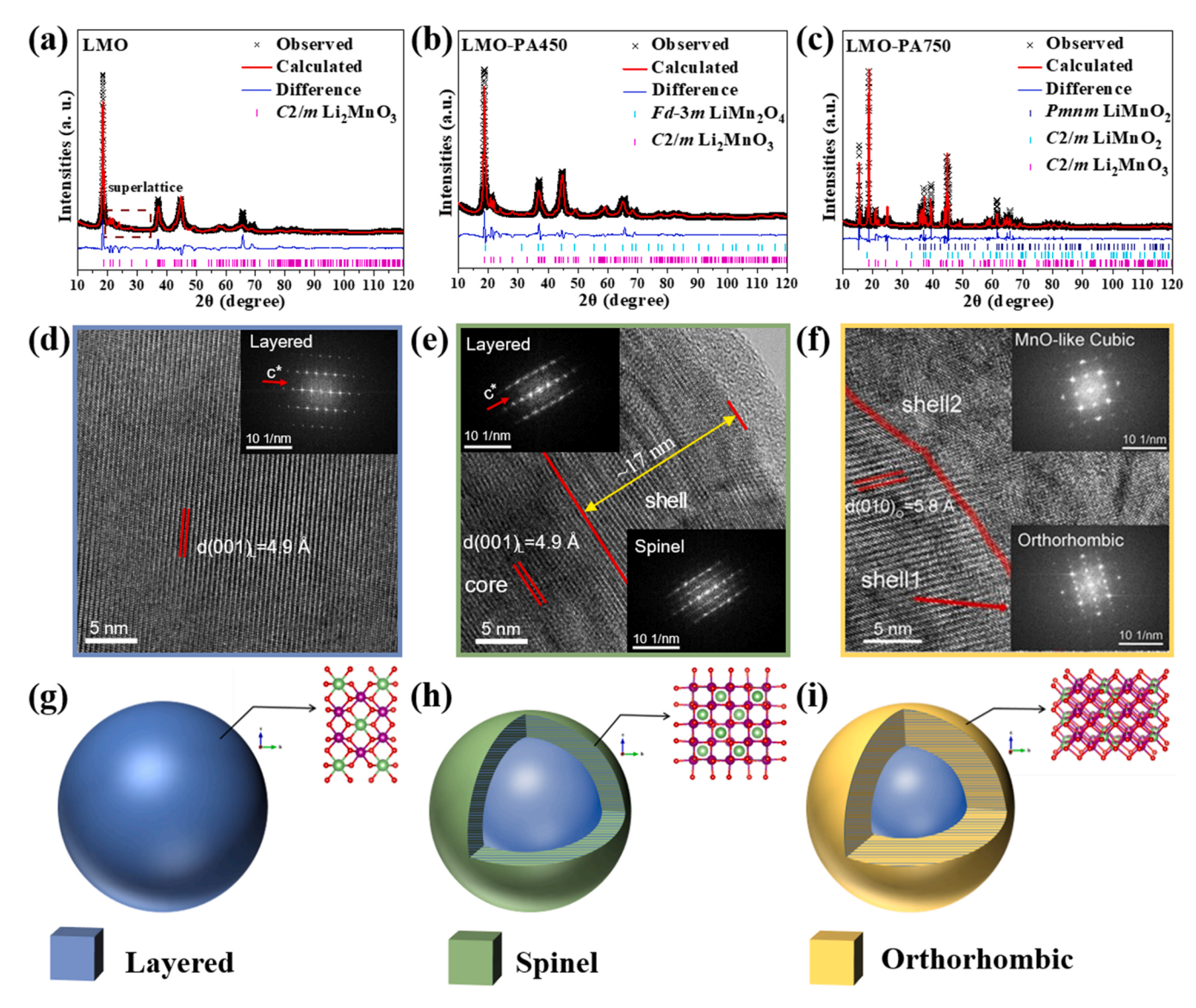


Fig. 4. XRD pattern and the Rietveld refinement of as-prepared LMO (a), LMO-PA450 (b), and LMO-PA750 (c). (d) HRTEM image of as-prepared LMO and the corresponding FFT map. (e) HRTEM image with selected-area FFT maps for LMO-PA450. (f) HRTEM image with selected-area FFT maps for LMO-PA750. Schematic illustration of as-prepared LMO (g), LMO-PA450 (h), and LMO-PA750 (i) with core-shell structural architecture.

structure. After annealing at 450 °C, except for the original Bragg diffraction peaks of the C2/m phase, a series of new peaks can be observed in the resulting XRD pattern (Fig. 4b). According to the Rietveld refinement, the composite (denoted as LMO-PA450) consists of two phases: 70.05 wt % C2/m layered phase and 29.95 wt % Fd-3m spinellike phase (Table S3). The morphology did not change noticeably compared with the pristine material (Fig. S7d). To verify the microstructure within single primary particles, we used the focused ion beam (FIB) to prepare samples for TEM. As shown in Fig. 4e, TEM image for LMO-PA450 can be divided into core and shell regions as indicated by a red line. As FFT maps in the insets show, the core still preserves the original layered phase, while the surface presents a spinel phase with a thickness of ~17 nm. The thickness is positively correlated with the calcinating time (Fig. S9). As the temperature further increased to 750 °C, the material exhibited a more complex XRD pattern (Fig. 4c). The Rietveld refinement shows that the composite (LMO-PA750) consists of three phases: 43.97 wt % C2/m Li₂MnO₃-like layered phase, 13.79 wt % C2/m LiMnO2-like layered phase, and 42.25 wt % Pmnm LiMnO₂-like layered phase (Table S3). As shown in Fig. S7g, the particles exhibit a lumpy shape with varying sizes. In the TEM image (Fig. 4f), the orthorhombic shell was confirmed by the typical (010) interplanar spacing and the corresponding FFT map (the outermost region is identified as a MnO-like cubic phase by the corresponding FFT map, labelled as "shell2"). The surface structure and the bulk structure of the LMO-PA750 were further examined in Fig. S10. The different d-spacings (5.8 Å for the (010) $_{\rm O}$ plane of the orthorhombic phase, and 4.9 Å for the (001) $_{\rm L}$ plane of the layered phase) and the different FFT patterns can distinguish the orthorhombic phase at the surface region and the layered phase in the bulk, indicating the formation of the core-shell structure. The structural schematics of LMO, LMO-PA450, and LMO-PA750 particles are displayed in Fig. 4g-i, respectively. The morphology change and the concurrent formation of the core-shell structures were illustrated in Fig. S8.

In the previous reports, most of the layered-spinel core-shell structure cathode materials were prepared by relatively complicated methods. Li's group used a water bath coupled with the high-temperature annealing and electrochemical process to get the LiCoO₂ cathode with a LiMn_{1.5}Ni_{0.5}O₄ spinel-like shell. [33] Cho's group prepared the Ni-rich layered oxide LiNi_{0.54}Co_{0.12}Mn_{0.34}O₂ with a Li_{1+x}(-CoNi_xMn_{2-x})₂O₄ spinel shell by sol-gel method followed with the annealing process at 800 °C. [34] Wu et al. used the sol-gel method coupled with an annealing process at 750 °C to synthesize a layered

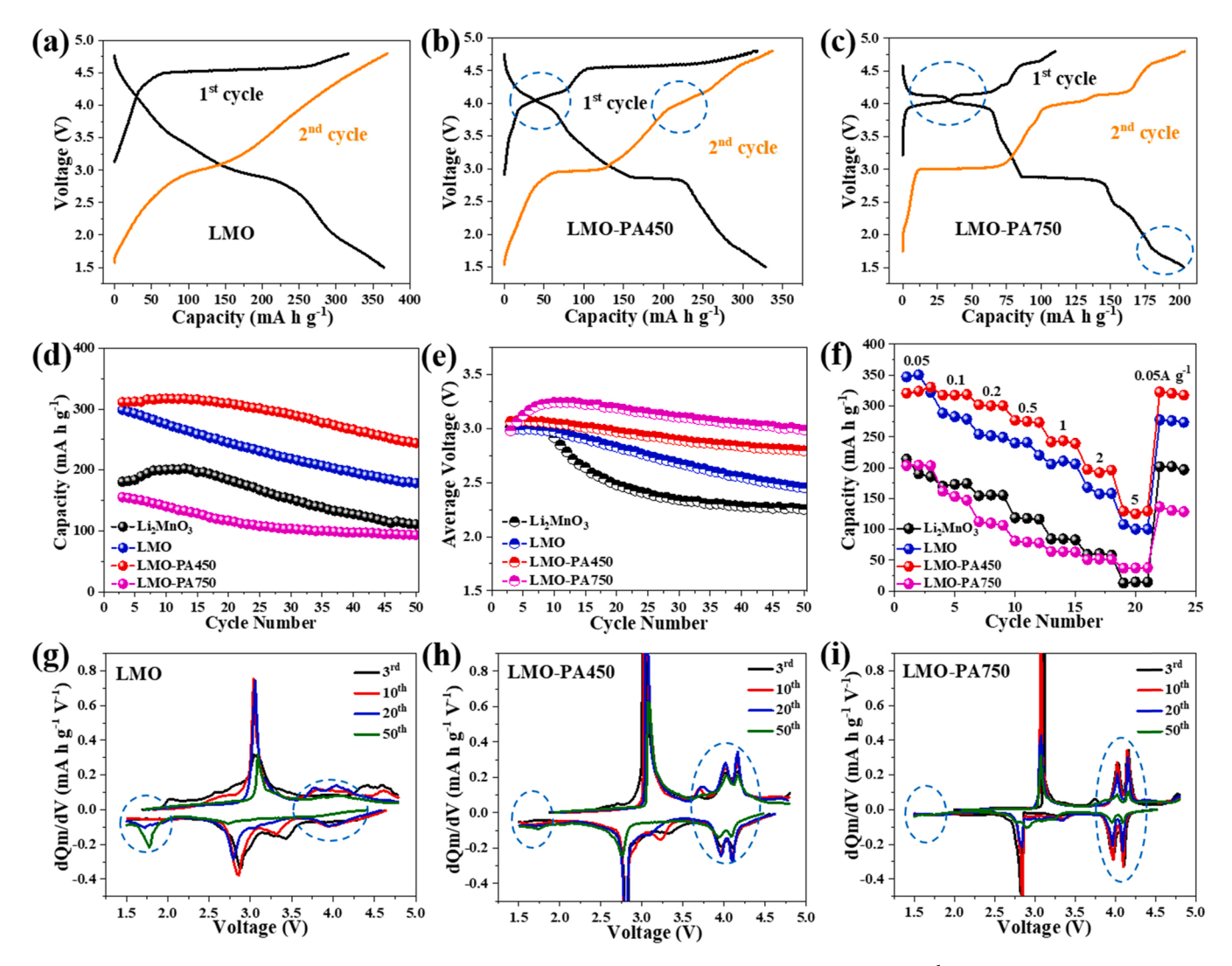


Fig. 5. The charge/discharge curves in the 1st cycle (black curves) and the 2nd cycle (yellow curves) at 25 °C and 10 mA g^{-1} for the samples LMO (a), LMO-PA450 (b), and LMO-PA750 (c). (d), (e) The cycling stability at 25 °C and 50 mA g^{-1} for the samples Li₂MnO₃, LMO, LMO-PA450, and LMO-PA750. (f) The rate capability at a different current density from 10 mA g^{-1} to 1000 mA g^{-1} for the sample Li₂MnO₃, LMO, LMO-PA450, and LMO-PA750. The dQ/dV curves of the sample LMO (g), LMO-PA450 (h), and LMO-PA750 (i) at the 3rd, 10th, 20th, and 50th cycles. (For interpretation of the references to colour in this figure legend, the reader is referred to the web version of this article.)

cathode $\mathrm{Li_{1.2}Ni_{0.2}Mn_{0.6}O_2}$ encapsulated by the spinel phase. [35] Guo's group prepared $\mathrm{Li_{1.2}Mn_{0.54}Co_{0.13}Ni_{0.13}O_2}$ coating with the $\mathrm{Li_4Mn_5O_{12}}$ spinel phase through dispersing the oxide precursors in KMnO₄ solution followed by an annealing process). [36] Moreover, most of the spinel shells above were achieved by the deposition of the second phase, which may result in the non-uniform surface coating. Here, in two types of core-shell structures for LMO-PA450 and LMO-PA750, the shells originated from the heat-induced structural evolution process, which can ensure the uniformity of the core-shell structures and the atom-level contact between shell and core.

2.4. Enhanced electrochemistry by tuning core-shell microstructure

The effects of these two core-shell structures on electrochemistry were demonstrated by assembling these materials as the cathode in coin cells. Fig. 5a-c shows the charge-discharge profiles in the voltage range of 1.5–4.8 V at a current density of 10 mA g^{-1} . As for the pristine LMO sample, there is a very long plateau above 4.5 V correlating with the typical O²⁻/O₂²⁻ redox reaction in the Li-rich layered oxides (Fig. 5a). Such a significant contribution from the oxygen redox reaction leads to an unprecedented high discharge capacity of above 360 mA h g^{-1} , which is higher than most of the reported Li-Mn-O system materials. In comparison, the curves for the LMO-PA450 with the spinel shell show a similar profile but a lower initial specific capacity of about 330 mA h g^{-1} (Fig. 5b). Differently, there is a pair of charge/discharge plateaus at about 4 V, marked by two blue dashed ellipses, which can be related to the de/intercalation of Li⁺ ions into the tetrahedral sites of the spinel structure. [37–40] As for the LMO-PA750 with the orthorhombic shell, the charge-discharge curves in Fig. 5c change a lot in contrast with that of the previous core-shell sample. The charge plateau of about 4 V becomes more obvious, and another discharge plateau appears in the potential range of 1.5-2.0 V, marked by two blue dashed ellipses, which can be associated with the formation of the new orthorhombic phase. [41–44] In addition, the initial specific capacity significantly decreases from > 300 mA h g⁻¹ to around 203 mA h g⁻¹, which may result from the serious Li and O loss during the phase transition process as well as the lower capacity of the orthorhombic phase. Fig. S11a-e presents the charge-discharge curves of the conventional Li-Mn-O Li-rich layered oxide Li₂MnO₃, LMO-PA350, LMO-PA550, LMO-PA650, LMO-PA850 samples. Fig. S12 exhibits the comparison of the cycling stability for Li₂MnO₃, pristine LMO, and other six post-annealing LMO samples at a current density of 10 mA g^{-1} . It can be found the LMO-PA450 maintained the highest reversible capacity > 270 mA h g after 20 cycles, while the LMO-PA750 showed superior cycling stability but a limited reversible specific capacity. Thus we mainly focused on the LMO-PA450 for further investigation. Figs. 5d and 5e present the comparison of the cycling stability for Li₂MnO₃, pristine LMO, LMO-PA450, and LMO-PA750 at the current density of 50 mA g⁻¹. It can be found that the LMO-PA450 shows enhanced cycling stability while still maintaining a high capacity of about 245 mA h g^{-1} , which should be related to the spinel shell. In addition, the LMO-PA450 shows the slowest average voltage fading when compared with the conventional Li₂MnO₃, pristine LMO, and LMO-PA750. The cycling stability of the three samples was also compared in the voltage range of 2.0-4.8 V, showing a similar trend (Fig. S13). To clarify the mechanism of the cycling stability for the LMO-PA450 sample, Fig. 5 h presents the dQ/dV curves of the 3rd, 10th, 20th, and 50th cycles. For comparison, Figs. S14, 5 g, and 5i display the dQ/dV curves of the 3rd, 10th, 20th, and 50th cycles for the conventional Li₂MnO₃, pristine LMO, and LMO-PA750 samples. The redox peaks at around 3.0 V in Figs. S14, 5 g, and 5i continuously shift to the opposite directions, accompanied by the fast decrease of peak areas. It is worth noting that the occurrence of redox peaks at around 4.0 V for conventional Li₂MnO₃ and pristine LMO samples indicate the irreversible phase transition from the layered phase to the spinel phase, while the fast attenuation of this peak could be related to the fast structure degradation by the formation spinel phase.

[45,46] In addition, the new redox peaks that occur at a low voltage region of about 1.7 V can well explain the severe average voltage fading. The LMO-PA450 in Fig. 5 h, shows great stability of the redox peaks at around 4 V and suppression of the peak at around 1.7 V, which should be responsible for the stable spinel shell. The rate capability of the conventional Li_2MnO_3 , pristine LMO, LMO-PA450, and LMO-PA750 was conducted at different current densities from 10 mA $\rm g^{-1}$ to 1000 mA $\rm g^{-1}$ (Fig. 5 f). The LMO-PA450 delivered a discharge capacity of about 330 mA h g⁻¹ at 10 mA g⁻¹ and even retained a discharge capacity of about 244 mA h $\rm g^{-1}$ at 200 mA $\rm g^{-1}$. For comparison, the conventional Li₂MnO₃ and pristine LMO only delivered a discharge capacity of about 85 and 210 mA h g⁻¹, respectively. DSC test was used to evaluate the thermal stability of the LMO-PA450 sample at Ar atmosphere. It can be observed the decomposition temperature is up to 300 °C, which is much higher than about 200 °C of the pristine sample (Fig. S15). In brief, tuning the core-shell structure with a suitable spinel shell exhibits enhanced cycling stability, rate capability and, structural stability.

2.5. Enhanced structural stability

To further explore the stability of LMO cathode materials with a coreshell structure, the in situ DEMS was conducted as a probe for the interfacial side reaction and lattice oxygen stability, and the corresponding results were shown in Fig. 6a-c. During the first charged process of the pristine LMO (Fig. 6a), both CO₂ and O₂ release started above 4.0 V, reflecting the serious interfacial electrolyte decomposition reaction and lattice oxygen loss. As for LMO-PA450, O2 released was greatly decreased, indicating the stability of the lattice oxygen has been greatly improved (Fig. 6b). In addition, there was no obvious CO₂ release can be observed in the LMO-PA450, indicating the suppressed interfacial side reaction between the spinel shell surface and carbonated electrolyte. In order to further prove the action of spinel shells, the in-situ DEMS was also conducted on LiMn₂O₄ spinel cathode. As shown in Fig. S16, there was no detectable CO2 and O2 release during the charging process, further confirming the improved interfacial structure stability in LMO-PA450 by the spinel shell. [47,48] For LMO-PA750, both CO₂ and O₂ release was greatly suppressed (Fig. 6c). The microstructural analysis of the above materials after 50 cycles were conducted by HRTEM images with the corresponding FFT patterns (Fig. 6d-f). The layered structure of LMO basically transformed to the spinel-like phase with the detectable lattice fringe distortion (Fig. 6d). On contrary, LMO-PA450 still preserved the original layered core-spinel shell structure even after long cycles, indicating the improved structural stability (Fig. 6e). As for LMO-PA750, the orthorhombic shell at particle surface transformed to a spinel-like structure, consistent with the previous reports. [44,49] We can deduce that the spinel-like surface structure is electrochemically favorable and stable for the Li-Mn-O system. In addition, XPS results (Fig. S17) show that Mn dissolution on Li anode after 50 cycles for LMO-PA450 is the smallest among three samples, which further confirms the enhancement of the core-shell structure on the electrochemical stability.

3. Conclusions

In this work, we systemically investigated the heat-induced structural evolution of a nonstoichiometric Li-Mn-O layered oxide combined with multiple macroscopic and microscopic characterization methods, as well as the effect of the structure on the electrochemistry. The continuous phase transition, from the original Li_2MnO_3 -like monoclinic phase to LiMn_2O_4 -like spinel phase, then to LiMn_2O_2 -like monoclinic and orthorhombic phases, was observed to occur at different temperatures in the bulk and at the surface of the primary particles, which are due to the different degrees of Li and O loss and the reduction of Mn. Most importantly, these heterogeneous phase transitions lead to two specific core-shell microstructures with either a spinel shell or an orthorhombic shell. The spinel shell was found to greatly enhance the cycling stability

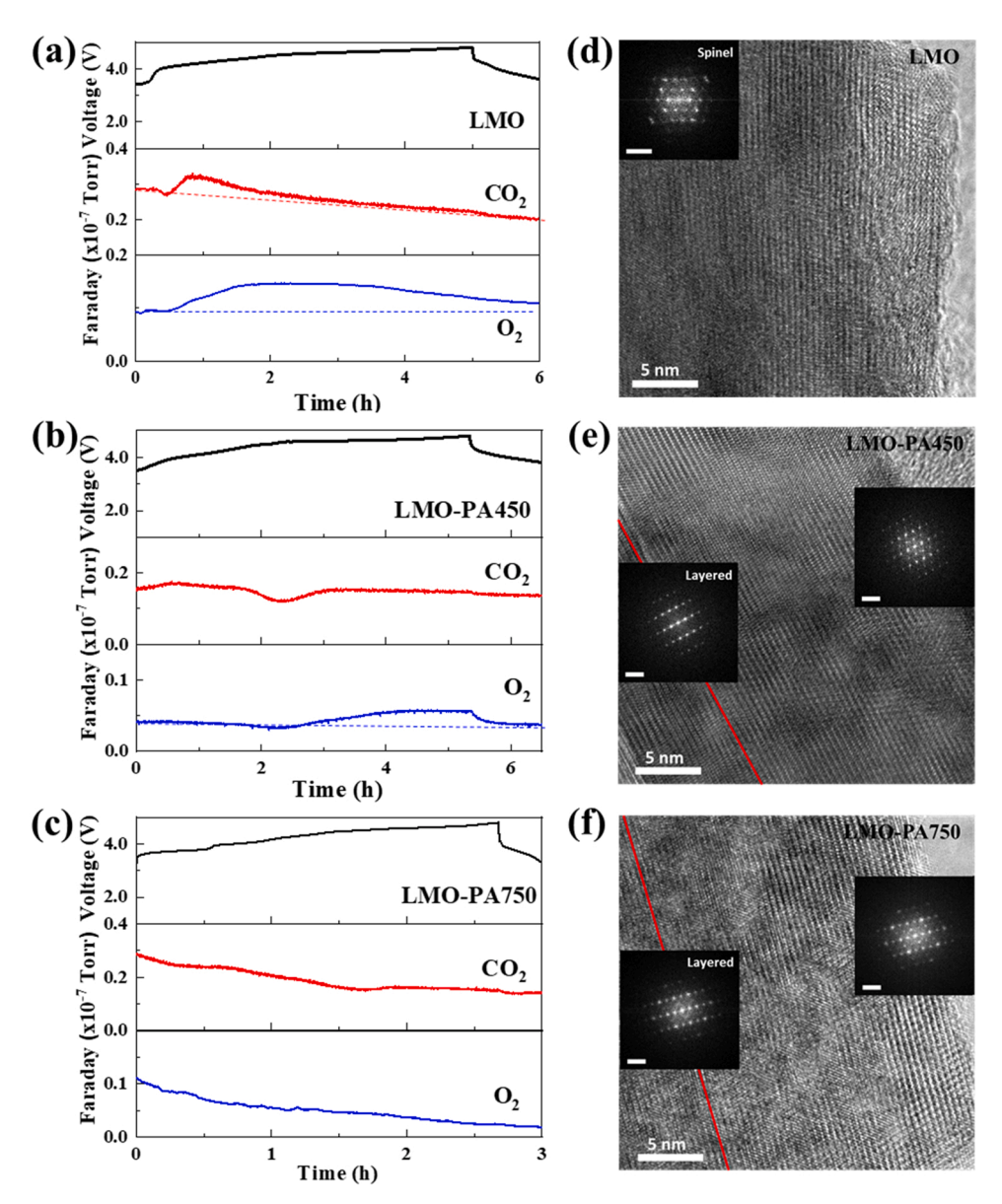


Fig. 6. (a-c) In situ DEMS results of LMO, LMO-PA450, and LMO-PA750 during the 1st cycle. (d-f) HRTEM patterns with the corresponding FFT images after 50 cycles.

of Li-Mn-O layered oxide. This work deepens our understanding of the phase structural evolution in the Li-Mn-O system and paves new pathways to design novel core-shell cathode materials with excellent electrochemical performance.

CRediT authorship contribution statement

Weiyuan Huang: Conceptualization, Investigation, Visualization, Methodology, Formal analysis, Writing – original draft. Xiaoyuan Li: Investigation, Visualization, Methodology, Formal analysis, Writing – original draft. Wenguang Zhao: Resources. Chen Zhu: Investigation. Hengyu Ren: Investigation. Haibiao Chen: Writing – review & editing. Feng Pan*: Writing – review & editing, Supervision, Project administration, Funding acquisition. Mingjian Zhang*: Conceptualization, Investigation, Visualization, Formal analysis, Writing – review & editing.

Declaration of Competing Interest

The authors declare that they have no known competing financial

interests or personal relationships that could have appeared to influence the work reported in this paper.

Acknowledgments

W. H. and X. L. contributed equally to this work. This work was financially supported by the National Natural Science Foundation of China (52172175), the Shenzhen Science and Technology Research Grant (JCYJ20200109140416788, JCYJ20210324130812033), the Chemistry and Chemical Engineering Guangdong Laboratory (1922018),the National Key R&D Program China (2020YFB0704500).

Appendix A. Supporting information

Supplementary data associated with this article can be found in the online version at doi:10.1016/j.nanoen.2022.107092.

References

- [1] P. He, H. Yu, D. Li, H. Zhou, J. Mater. Chem. 22 (2012) 3680.
- [2] J.K. Kim, A. Manthiram, Nature 390 (1997) 265.
- [3] M. Freire, N.V. Kosova, C. Jordy, D. Chateigner, O.I. Lebedev, A. Maignan, V. Pralong, Nat. Mater. 15 (2016) 173.
- [4] M.M. Thackeray, M.F. Mansuetto, J.B. Bates, J. Power Sources 68 (1997) 153.
- [5] J. Zhao, Y. Wang, Nano Energy 2 (2013) 882.
- [6] T. Liu, A. Dai, J. Lu, Y. Yuan, Y. Xiao, L. Yu, M. Li, J. Gim, L. Ma, J. Liu, C. Zhan, L. Li, J. Zheng, Y. Ren, T. Wu, R. Shahbazian-Yassar, J. Wen, F. Pan, K. Amine, Nat. Commun. 10 (2019) 4721.
- [7] M. Oishi, C. Yogi, I. Watanabe, T. Ohta, Y. Orikasa, Y. Uchimoto, Z. Ogumi, J. Power Sources 276 (2015) 89.
- [8] M. Saubanere, E. McCalla, J.M. Tarascon, M.L. Doublet, Energy Environ. Sci. 9 (2016) 984.
- [9] A.R. Armstrong, M. Holzapfel, P. Novak, C.S. Johnson, S.-H. Kang, M. M. Thackerav, P.G. Bruce, J. Am. Chem. Soc. 128 (2006) 8694.
- [10] W.E. Gent, K. Lim, Y. Liang, Q. Li, T. Barnes, S.-J. Ahn, K.H. Stone, M. McIntire, J. Hong, J.H. Song, Y. Li, A. Mehta, S. Ermon, T. Tyliszczak, D. Kilcoyne, D. Vine, J.-H. Park, S.-K. Doo, M.F. Toney, W. Yang, D. Prendergast, W.C. Chueh, Nat. Commun. 8 (2017) 2091.
- [11] F. Capitaine, P. Gravereau, C. Delmas, Solid State Ion. 89 (1996) 197.
- [12] J.M. Paulsen, C.L. Thomas, J.R. Dahn, J. Electrochem. Soc. 146 (1999) 3560.
- [13] A.R. Armstrong, P.G. Bruce, Nature 381 (1996) 499.
- [14] X. Zhu, F. Meng, Q. Zhang, L. Xue, H. Zhu, S. Lan, Q. Liu, J. Zhao, Y. Zhuang, Q. Guo, B. Liu, L. Gu, X. Lu, Y. Ren, H. Xia, Nat. Sustain 4 (2021) 392.
- [15] H. Shang, Y. Zuo, F. Shen, J. Song, F. Ning, K. Zhang, L. He, D. Xia, Nano Lett. 20 (2020) 5779.
- [16] X. Cao, H. Li, Y. Qiao, M. Jia, X. Li, J. Cabana, H. Zhou, Adv. Mater. 33 (2021) 2004280
- [17] S. Gao, T. Yang, H. Zhang, D. Song, X. Shi, L. Zhang, J. Alloy. Compd. 729 (2017) 695.
- [18] D. Kong, M. Zhang, Y. Xiao, J. Hu, W. Zhao, L. Han, F. Pan, Nano Energy 59 (2019) 327.
- [19] A. Manthiram, B. Song, W. Li, Energy Storage Mater. 6 (2017) 125.
- [20] J. Zheng, T. Liu, Z. Hu, Y. Wei, X. Song, Y. Ren, W. Wang, M. Rao, Y. Lin, Z. Chen, J. Lu, C. Wang, K. Amine, F. Pan, J. Am. Chem. Soc. 138 (2016) 13326.
- [21] D. Mohanty, J. Li, D.P. Abraham, A. Huq, E.A. Payzant, D.L. Wood III, C. Daniel, Chem. Mater. 26 (2014) 6272.
- [22] M. Gu, I. Belharouak, J. Zheng, H. Wu, J. Xiao, A. Genc, K. Amine, S. Thevuthasan, D.R. Baer, J.-G. Zhang, N.D. Browning, J. Liu, C. Wang, ACS Nano 7 (2013) 760.
- [23] P. Yan, A. Nie, J. Zheng, Y. Zhou, D. Lu, X. Zhang, R. Xu, I. Belharouak, X. Zu, J. Xiao, K. Amine, J. Liu, F. Gao, R. Shahbazian-Yassar, J.-G. Zhang, C.-M. Wang, Nano Lett. 15 (2015) 514.
- [24] W. Hua, M. Chen, B. Schwarz, M. Knapp, M. Bruns, J. Barthel, X. Yang, F. Sigel, R. Azmi, A. Senyshyn, A. Missiul, L. Simonelli, M. Etter, S. Wang, X. Mu, A. Fiedler, J.R. Binder, X. Guo, S. Chou, B. Zhong, S. Indris, H. Ehrenberg, Adv. Energy Mater. 9 (2019) 1803094.
- [25] H. Yu, Y.-G. So, Y. Ren, T. Wu, G. Guo, R. Xiao, J. Lu, H. Li, Y. Yang, H. Zhou, R. Wang, K. Amine, Y. Ikuhara, J. Am. Chem. Soc. 140 (2018) 15279.
- [26] D. Wang, R. Yu, X. Wang, L. Ge, X. Yang, Sci. Rep. 5 (2015) 8403.
- [27] S.J. Hwang, H.S. Park, J.H. Choy, G. Campet, J. Phys. Chem. B 104 (2000) 7612.
- [28] N. Faenza, L. Bruce, Z. Lebens-Higgins, I. Plitz, N. Pereira, L. Piper, G. Amatucci, J. Electrochem. Soc. 164 (2017) A3727.
- [29] G. Amatucci, J. Tarascon, D. Larcher, L. Klein, Solid State Ion. 84 (1996) 169.
- [30] D. Larcher, M. Palacin, G. Amatucci, J. Tarascon, J. Electrochem. Soc. 144 (1997) 408.
- [31] W. Lee, S. Lee, E. Lee, M. Choi, R. Thangavel, Y. Lee, W. Yoon, Energy Storage Mater. 44 (2022) 441.
- [32] J. Park, B. Choi, Y. Kang, S. Park, D. Yun, I. Park, J. Shim, J. Park, H. Han, K. Park, Energy Technol. 6 (2018) 1361.
- [33] Z. Zhu, D. Yu, Z. Shi, R. Gao, X. Xiao, I. Waluyo, M. Ge, Y. Dong, W. Xue, G. Xu, W. K. Lee, A. Hunt, J. Li, Energy Environ. Sci. 13 (2020) 1865.
- [34] Y. Cho, S. Lee, Y. Lee, T. Hong, J. Cho, Adv. Energy Mater. 1 (2011) 821.
- [35] F. Wu, N. Li, Y. Su, L. Zhang, L. Bao, J. Wang, L. Chen, Y. Zheng, L. Dai, J. Peng, S. Chen, Nano Lett. 14 (2014) 3550.
- [36] X.-D. Zhang, J.-L. Shi, J.-Y. Liang, Y.-X. Yin, J.-N. Zhang, X.-Q. Yu, Y.-G. Guo, Adv. Mater. 30 (2018) 1801751.
- [37] X. Zhang, H. Zheng, V. Battaglia, R.L. Axelbaum, J. Power Sources 196 (2011) 3640.
- [38] W. Liu, G.C. Farrington, F. Chaput, B. Dunn, J. Electrochem. Soc. 143 (1996) 879.
- [39] D.K. Kim, P. Muralidharan, H.-W. Lee, R. Ruffo, Y. Yang, C.K. Chan, H. Peng, R. A. Huggins, Y. Cui, Nano Lett. 8 (2008) 3948.
- [40] J. Cho, M.M. Thackeray, J. Electrochem. Soc. 146 (1999) 3577.
- [41] I. Koetschau, M.N. Richard, J.R. Dahn, J.B. Soupart, J.C. Rousche, J. Electrochem. Soc. 142 (1995) 2906.
- [42] X. Li, Z. Su, Y. Wang, J. Alloy. Compd. 735 (2018) 2182.
- [43] G.X. Wang, P. Yao, S. Zhong, D.H. Bradhurst, S.X. Dou, H.K. Liu, J. Appl. Electrochem 29 (1999) 1423.
- [44] R.J. Gummow, M.M. Thackeray, J. Electrochem. Soc. 141 (1994) 1178.
- [45] J.R. Croy, D. Kim, M. Balasubramanian, K. Gallagher, S.-H. Kang, M.M. Thackeray, J. Electrochem. Soc. 159 (2012) A781.
- [46] S.H. Kang, P. Kempgens, S. Greenbaum, A.J. Kropf, K. Amine, M.M. Thackeray, J. Mater. Chem. 17 (2007) 2069.

- [47] X.-D. Zhang, J.-L. Shi, J.-Y. Liang, Y.-X. Yin, J.-N. Zhang, X.-Q. Yu, Y.-G. Guo, Adv. Mater. 30 (2018) 1801751.
- [48] S. Zhang, J. Chen, T. Tang, Y. Jiang, G. Chen, Q. Shao, C. Yan, T. Zhu, M. Gao, Y. Liu, H. Pan, J. Mater. Chem. A 6 (2018) 3610.
- [49] I.J. Davidson, R.S. McMillan, J.J. Murray, J.E. Greedan, J. Power Sources 54 (1995) 232.



Weiyuan Huang received his B.S. degree from South China Normal University in 2017. He is pursuing his Ph.D. degree in the School of Advanced Materials, Peking University, China. His research interests mainly focus on cathode materials for lithium ion batteries and sodium ion batteries, especially on layered oxide materials including Mn-rich layered oxides and high voltage LiCoO₂ layered oxides.



Xiaoyuan Li received his B.S. degree from Harbin Institute of Technology in 2019. He is pursuing his M.S. degree in the School of Advanced Materials, Peking University, China. His research interests mainly focus on cathode materials for lithium ion batteries, especially on layered oxide materials including Mn-rich layered oxides.



Wenguang Zhao is an engeneer in the School of Advanced Materials, Peking University Shenzhen Graduate School, China. He has over 10 years' experience in material characterization using wide range of analytical tools including XRD, XPS, SEM and TEM. His research interests mainly focus on the Ex/in-situ TEM and Ex/in-situ XRD characterization of battery materials.



Chen Zhu received her B.S. degree from Central South University in 2020. She is pursuing her M.S. degree in the School of Advanced Materials, Peking University, China. Her research interests mainly focus on characterization methods of nanoenergy materials, especially the development and application of in-site observation techniques.



Hengyu Ren received his B.S. degree from Dalian University of Technology in 2020. He is pursuing his M.S. degree in the School of Advanced Materials, Peking University, China. His research interests mainly focus on cathode materials for lithium ion batteries, especially on layered oxide materials including Mn-rich layered oxides and high voltage ${\rm LiCoO}_2$ layered oxides.



Dr. Feng Pan, founding Dean of School of Advanced Materials, Peking University Shenzhen Graduate School, got B.S. from Dept. Chemistry, Peking University in 1985 and Ph.D. from Dept. of P&A Chemistry, University of Strathclyde, Glasgow, UK, with "Patrick D. Ritchie Prize" for the best Ph.D. in 1994. With more than a decade experience in large international incorporations, Prof. Pan has been engaged in fundamental research and product development of novel optoelectronic and energy storage materials and devices. As Chief Scientist, Prof. Pan led eight entities in Shenzhen to win 150 million RMB grant for the national new energy vehicles (power battery) innovation project since 2013.



Haibiao Chen is currently a senior researcher at School of Advanced Materials, Peking University Shenzhen Graduate School. He received his Bachelor's degree from Tsinghua University in 2000 and PhD from Stevens Institute of Technology in 2006. He worked at Velocys during 2006–2011 and UES during 2011–2014.



Dr. Mingjian Zhang got his Ph.D. degree from Fujian Institute of Research on the Structure of Matter, Chinese Academy of Sciences in 2013, then worked there as an assistant research fellow for one year. From 2014–2018, he was a postdoc in School of Advanced Materials, Peking University, and became an assistant research professor in 2018–2020, and promoted to an associate research professor since 2021. Meanwhile, he was a research scholar in Brookhaven National Lab from 2016 to 2019, then in the University of Chicago in 2019. He has been engaged in the fields of high-performance cathode materials for Li-ion batteries, especially the structural evolution and structure-property research of the cathodes.